Modeling, Identification and Control, Vol. 35, No. 2, 2014, pp. 109–125, ISSN 1890–1328

Gear fatigue damage for a 500 kW wind turbine exposed to increasing turbulence using a flexible multibody model

M. F. Jørgensen [1] N. L. Pedersen [1] J. N. Sørensen [2]

[1] *Dept. of Mech. Eng., Technical University of Denmark, DK-2800 Lyngby, Denmark. E-mail: mfjo@mek.dtu.dk, nlp@mek.dtu.dk*

[2] *Dept. of Wind Energy, Technical University of Denmark, DK-2800 Lyngby, Denmark. E-mail: jnso@dtu.dk*

Abstract

This paper investigates gear tooth fatigue damage in a 500 kW wind turbine using FLEX5 and own multibody code. FLEX5 provides the physical wind field, rotor and generator torque and the multibody code is used for obtaining gear tooth reaction forces in the planetary gearbox. Different turbulence levels are considered and the accumulated fatigue damage levels are compared. An example where the turbulence/fatigue sensitivity could be important, is in the middle of a big wind farm. Interior wind turbines in large wind farms will always operate in the wake of other wind turbines, causing increased turbulence and therefore increased fatigue damage levels. This article contributes to a better understanding of gear fatigue damage when turbulence is increased (e.g. in the center of large wind farms or at places where turbulence is pronounced).

Keywords: gearbox, geartooth, gearteeth, turbulence, multibody, wind turbine, fatigue

1 Introduction

Gearbox failures and emergency stops caused by drivetrain problems are very expensive for the wind turbine industry. Drivetrain components are critical for operation, they're typically large, heavy and expensive to repair or replace. Costs for operation and maintenance (O&M) increase by the time wind turbines are non-producing. Component lifetime reliability is important. A key parameter to designing drivetrain components is calculation (estimation) of accumulated fatigue damage. Related problems during the lifetime of a wind turbine are issues with corrosion, wear and leading edge blade erosion, which can reduce the performance.

The efficiency of wind turbines is continously being improved in order to decrease the total cost of energy and therefore it is important to be able to investigate the fatigue damage under different circumstances. One way of dealing with fatigue problems is mechanical: Changing the design, increasing safety factors, dimensions etc. Another method is by developing or improving wind turbine controller mechanisms. Wind turbines are complicated machines with a lot of electrical equipment such as controllers for automatic adjustment of e.g. pitch/yaw regulation. In Molinas et al. (2010) an indirect torque control (ITC) technique has been investigated and the idea is that electromagnetic torque transients caused by grid faults and disturbances results in significant gearbox fatigue. As demonstrated in Schlechtingen et al. (2013) there is also a lot of development going on in the field of "condition monitoring" which include recording large amounts of data using sensors for e.g. oil temperature, wind/rotor/generator speed, vibration/accelerometers,

doi:10.4173/mic.2014.2.4

current and power output etc., which is then processed for early diagnosis of problems.

Fatigue loads for rotor and main gearbox bearings are calculated in Heege et al. (2007) using a method that couples non-linear Finite Element Method (FEM) and super element technique with a multibody approach (see e.g. Haug (1989); Géradin and Cardona (2001)). An approach to predicting wind turbine gearbox reliability for three generic gearbox configurations, based on assumptions of estimated failure rates, is given in Smolders et al. (2010)

The most common cause of gearbox failure is surface contact fatigue (see Fernandes and McDuling (1997) which also presents examples and describes rolling contact fatigue, sliding-rolling contact fatigue and spalling). Recently, researchers from National Renewable Energy Laboratory (NREL) initiated the Gearbox Reliability Collaborative (GRC) and guarantee privacy of commercially sensitive information, see Musial et al. (2007) in order to investigate gearbox problems and seek solutions that will lead to higher gearbox reliability.

A description of four stages of fatigue damage from initial crack to failure is given in Vasudevan et al. (2001), which also provides an overview of the topic from a historical perspective together with suggestions for the concept of fatigue damage control.

A typical procedure for fatigue load data analysis for wind turbine gearboxes is given in Niederstucke et al. (2003). In this article the commercial software package FLEX5 Øye (2001) will be used for obtaining wind turbine loads (forces and torque). The focus will be on investigating gear tooth fatigue, using a multibody dynamics program developed in Matlab. The gear tooth stresses are found using either Comsol Multiphysics Multiphysics (1998-2012) or empirical calculated Hertzian contact stresses. A Matlab rainflow counting program (RFC) is used for determining the fatigue damage, based on an estimated Wöhler-curve. The gear teeth are modeled as flexible and the discontinuous nature of the stiffness is included.

1.1 Proposed Method

Figure 1 demonstrates the concept of this article, which is to calculate gear tooth fatigue based on turbulent wind input.

Accumulated fatigue damage for a wind turbine producing power using wind speed from 6-20 m/s and a bin size of 2 m/s will be investigated (the 6 m/s bin contains wind speeds from 5-7 m/s etc.). Based on Jørgensen et al. (2014b) the turbulence intensity (TI) is set to around 10-20% throughout the whole interval. For this particular site the Weibull parameters based on 5 years of wind data from Hansen and Larsen

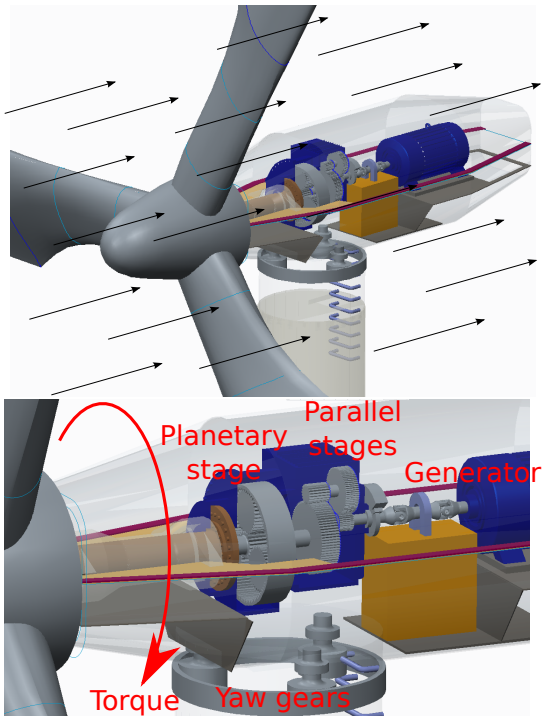

Figure 1: Wind turbine subject to a given wind field with illustration of main shaft torque, driving the carrier and planets in the gearbox, for generating power through the generator.

(1997-2011) are calculated. The parameters have been extrapolated to hub height at 36 m and Seguro and Lambert (2000) provide a description of how to perform this using the (1) maximum likelihood method, (2) a modified maximum likelihood method and (3) a graphical method. The Weibull cumulative distribution function Seguro and Lambert (2000) is given by

$$P(v < v_i) = P(v \geq 0)\left\{1 - \exp\left[-\left(\frac{v_i}{A}\right)^k\right]\right\} \quad (1)$$

where $P(v \geq 0)$ is the probability that the wind speed equals or exceeds zero while $P(v < v_i)$ is the probability that the wind speed is below v_i. Weibull parameters for this site is estimated to $A = 6.62$ and $k = 2.19$ using 5 years of measurement data. The rated lifetime is 20 years or approximately $(20 \cdot 365 \cdot 24) = 175200$ hours but the wind turbine does not run all the time as seen in Table 1 (approximately 60% of the time).

The aerodynamic tool FLEX5 and a multibody program is used for obtaining the gear tooth loads under representative and realistic conditions, however these simulations are rather short compared to the timescales in Table 1. Therefore it is important to ensure the statistical behavior of the simulation input and output as simulation results will be extrapolated to a lifetime

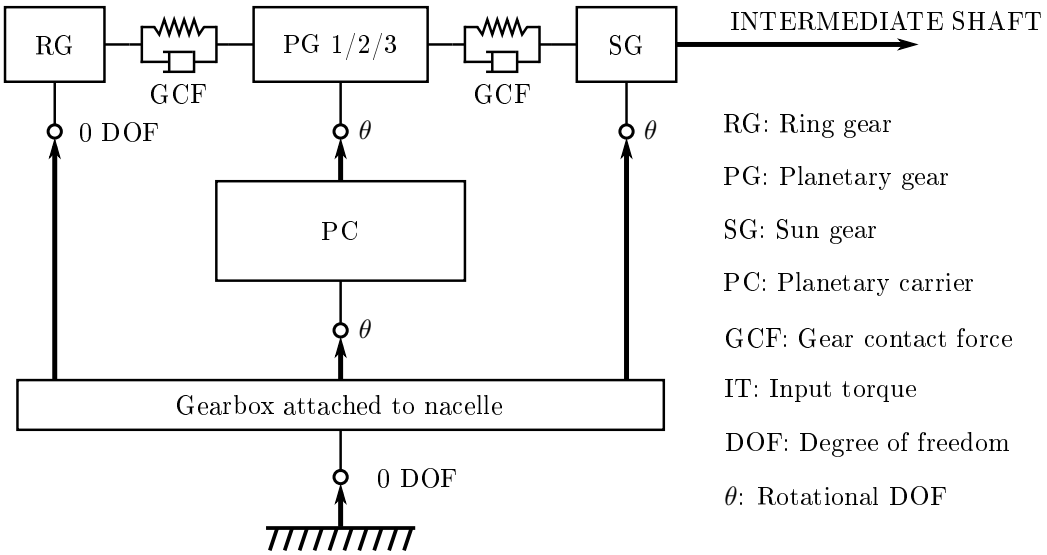

Figure 2: Topology diagram of the Matlab multibody gearbox model (as illustrated in Dong et al. (2012)).

Wind speed [m/s]	6	8
In operation [hours]	45418	31900

10	12	14	16	18	20
16320	6189	1751	370	58	7

Table 1: Hours of operation at different wind speeds (binned). Total operation is 102013 hours.

operation of 20 years.

For the multibody program, a similar procedure as in Dong et al. (2012) with topology diagram shown in Figure 2 will be employed. Instead of using data from the NREL (GRC) 750 kW wind turbine Musial et al. (2007), data from a 500 kW planetary gearbox will be used. For aerodynamics FLEX5 instead of FAST is used. Our own multibody code instead of SIMPACK is used and rainflow counting and Palmgren-Miner summation is made with Matlab.

1.2 Wake effects and turbulence in wind farms

The inflow to wind turbines is always turbulent. This puts a special demand on the modelling of the incoming wind, as it is required to model not only the mean properties of the flow field, but also the turbulence characteristics. A practical way to model turbulence is to assume it to be homogeneous and letting it obey some simplified constraints with respect to e.g. turbulence intensity and a predefined length scale. This enables one to develop models for generating synthetic turbulence that to a large extent mimics the real behaviour of turbulence. Examples of such models applied within the field of wind energy are the model of Veers (1988), which only depend on single point power spectral densities and a coherence function, or the model of Mann (1998), which also takes into account dissipative characteristics. The description becomes somewhat more complicated when wind turbines are clustered in wind farms, where the turbulence intensity increases due to the mutual interaction between the wakes of the turbines. This is an inherent, albeit unwanted effect, which designers of wind turbines also have to deal with.

Wind turbines are mainly positioned in wind farms in order to limit the overall installation and maintenance expenses. The price to pay, however, is that wake effects cause a decrease in total power production as well as an increase in the self-generated turbulence, which, as a consequence, results in life-time reductions. Hence, in order to design and optimize wind turbines for use in wind farms, it is required to superpose the mean wind field with turbulence corresponding to what is encountered by the turbine. The problem is best illustrated in Figure 3, which shows a photo of the flow field inside the Horns Rev wind farm. The photo, which was taken an early morning, shows the turbulence generation due to the mixing of wakes visualized through condensation of water drops. The first turbines in the wind farm are seen to only subject to the turbulence of the incoming wind, whereas the remaining turbines are subject both to the ambient turbulence and the additional turbulence generated by the wakes of the surrounding turbines. This increases the overall turbulence level and causes the turbulence to become anisotropic. In the interior of the farm, the turbulence settles at a constant level and, due to mix-

Figure 3: Wake effects (photograph of the Horns Rev 1 offshore wind farm, Hasager et al. (2013)).

ing of surrounding wakes, it becomes approximately homogeneous. Thus, in the interior of a wind farm it is again possible to employ simplified turbulence models for generating synthetic turbulence for use in aerodynamic/structural dynamic models. In the present work we employ the wind simulation model of Veers (1988) to generate isotropic synthetic turbulence. The model is implemented in the aeroelastic code FLEX5 and only utilizes the turbulence intensity as input. For more information about the model, we refer to the original report.

Another way of expressing the importance of wake-induced turbulence as shown in Figure 3 is by directly measuring the wind field and blade loads. Experimental data from e.g. the Vindeby wind farm (south of Denmark), clearly shows that the standard deviation of the turbulence and wind loads (flap-wise bending moment) increase when wind turbines appear in the wake of other wind turbines ((Tronæs Frandsen, 2007, Fig. 1.2, 1.3)). Because load peaks due to wake effects are clearly visible, it is obvious to link turbulence level and fatigue loadings. The question about how turbulence affects individual wind turbines, has large influence on the relevance of this work for wind turbine gearboxes in a wind farm.

1.3 Fatigue damage

Employing S–N or Wöhler curves is a suitable approach that is generally accepted for fatigue lifetime estimation. The idea of the chosen method is to use a rainflow counting algorithm on the gear tooth stress time-series. The result is a measure of cycle amplitudes or ranges which can be counted in bins and collected in a rainflow matrix, which is a function of mean values and ranges. See e.g. Madsen (1990) for a description of the rainflow counting algorithm, which together with the linear Palmgren-Miner rule, based on Palmgren (1924) and Miner (1945) forms the following important relationships

$$D = \sum_{i=1}^{j} \frac{n_i}{N_i} = \sum_{i=1}^{j} n_i \frac{S_i^m}{S_0^m}, \tag{2}$$

$$\log S_i = \log S_0 - \frac{1}{m} \log N_i \quad \Rightarrow \quad S_i = \frac{S_0}{N_i^{1/m}} \tag{3}$$

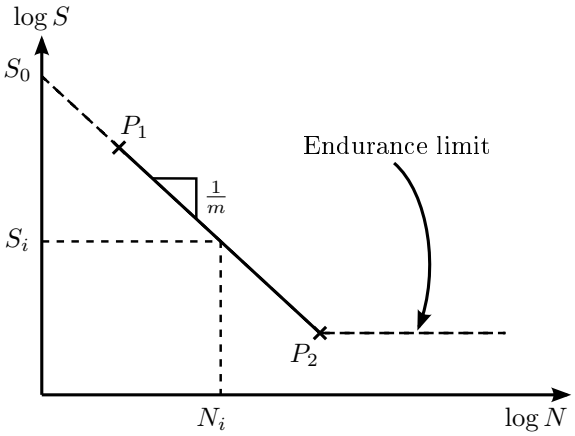

Figure 4: S–N-curve for fatigue damage.

Equation (2) states the accumulated fatigue damage, also known as the linear damage hypothesis. Generally the material/component will fail when the sum $D >= 1$. At stress level number i, the number of counted cycles n_i is a result of the rainflow counting algorithm evaluated on the time series. The algorithm returns the range (or amplitude) of all stresses for the i^{th} case, i.e. (n_i, s_i). Capital N_i is the maximum number of cycles to failure and also shown in Figure 4.

Equation (3) describes the curve in Figure 4 and $1/m$ is the slope in the loglog-plot. The m is the damage exponent, describing the rate of change in maximum allowed stress as the cycle count changes. This exponent is typically 3-3.5 for steel, 7 for cast iron and 10-20 for glass- and carbon-fiber component materials.

Lifetime predictions cannot alone be based on this, because the S–N-curve is typically based on statistical

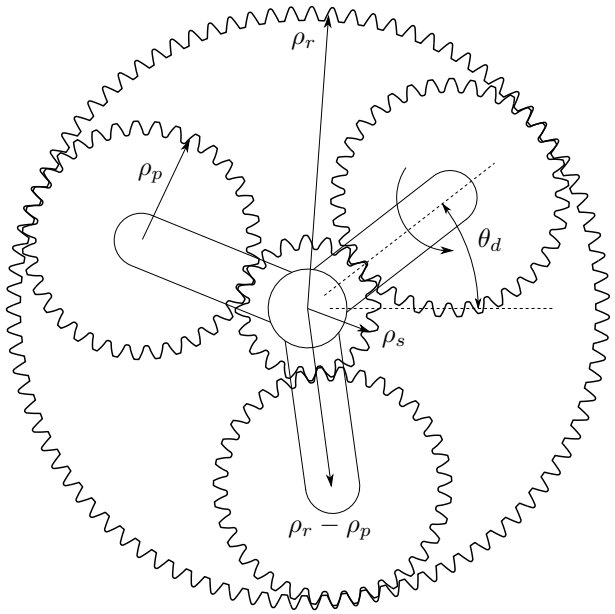

Figure 5: Planetary gearbox with radii for sun ρ_s, planet (ρ_p) and ring (ρ_r) gears. Planetary carrier (driver) angle is θ_d.

data based on small-scale experiments and the S–N-curve itself is associated with large uncertainties where the safety factor would be based on empirical values. Accurate information about the S–N-curve for huge wind turbine components like the gears described in the present article, is assumed to be known. The gear root bending stresses are obtained using Finite Element Modelling (FEM) using Comsol Multiphysics Multiphysics (1998-2012). Surface stresses are considered as well and calculated using Hertzian contact stresses Norton (2000).

2 Planetary gearbox model

The following section describes planetary gearbox details (tooth data and facewidth etc.) followed by a description of the implemented multibody code for obtaining gear tooth forces and stresses.

The number of teeth in the first (planetary) gearbox stage is 20, 35 and 91 for respectively the sun, planet and ring gears. The profile shift is $x_s = 0.582$, $x_p = 0.419$ and $x_r = -0.840$, respectively. Minimum contact facewidth for sun/planet and planet/ring is 210 mm. It is assumed that bearings and wind turbine model components are rigid such that the gear tooth forces depend on axial rotor and generator torque, regardless of transverse forces and torque (a 2D model). A real wind turbine and gearbox which has been running since 1995 is considered. It is therefore expected that the calculated accumulated fatigue, D in Equation (2), for 20 years of operation should be acceptable.

2.1 Multibody program code

Multibody dynamics software is used to couple or link mechanical rigid or elastic bodies with each other. General introductions to the field are given in e.g. Nikravesh (1988); Shabana (1989); Géradin and Cardona (2001). Equations of motion are expressed using the following n differential equations coupled with m algebraic equations

$$\begin{cases} \mathbf{M}\ddot{\mathbf{q}} - \mathbf{\Phi}_\mathbf{q}^\mathbf{T}\boldsymbol{\lambda} = \mathbf{g}, & \mathbf{\Phi}_\mathbf{q} = \dfrac{\partial \mathbf{\Phi}}{\partial \mathbf{q}} \\ \mathbf{\Phi}(\mathbf{q}, t) = \mathbf{0} \end{cases} \tag{4}$$

where $\mathbf{M} \in \mathbb{R}^{n\times n}$ is the mass/inertia matrix, $\mathbf{q} \in \mathbb{R}^n$ is a vector of cartesian coordinates, $\mathbf{\Phi}_\mathbf{q} \in \mathbb{R}^{m\times n}$ is the Jacobian of the $\mathbf{\Phi}(\mathbf{q}, t) \in \mathbb{R}^m$ kinematic constraint equations, $\boldsymbol{\lambda} \in \mathbb{R}^m$ are the the Lagrange multipliers and $\mathbf{g} \in \mathbb{R}^n$ are the external body forces applied in the global reference system. For the model here the primary input is the load. At one end the rotor torque is applied and on the other end of the transmission system the torque from the generator is applied. The model load input is the output generated by the FLEX5 program. Constraint equations in the $\mathbf{\Phi}(\mathbf{q}, t)$-vector are expressed at acceleration level, to form equations of motion from the DAE-system (4) into an ODE in the form given by Nikravesh (1988):

$$\begin{bmatrix} \mathbf{M} & -\mathbf{\Phi}_\mathbf{q}{}^T \\ \mathbf{\Phi}_\mathbf{q} & \mathbf{0} \end{bmatrix} \begin{Bmatrix} \ddot{\mathbf{q}} \\ \boldsymbol{\lambda} \end{Bmatrix} = \begin{Bmatrix} \mathbf{g} \\ \boldsymbol{\gamma} \end{Bmatrix} \tag{5}$$

Force elements (springs and dampers) are used to model the connecting flexibility between rigid gears, instead of using (rigid) gear constraints. A full description of the applied force element algorithms as illustrated by Figure 2 is presented in Jørgensen et al. (2014a), where it is compared to a method using a constraint formulation instead.

The force element algorithm requires knowledge of the total gear tooth force, i.e. the sum of the gear tooth forces on either one or two teeth. Fatigue is a local phenomenon in single points so knowledge of the force, i.e. magnitude and direction and where it is acting on a single tooth is required. The main specific points of interest are either at the gear root or at the tooth surface contact point. The difference between obtaining and storing the force acting on a single tooth instead of the total gear force, can be regarded as a matter of calculating a mesh stiffness ratio and then internally store the mesh stiffness of a single tooth. This method is described in details in Jørgensen et al. (2014a). The force acting on a single tooth is found by using Hooke's

law, by multiplying the tooth penetration depth and the stiffness from the multibody code.

2.2 Details of constraint functions

A planetary gearbox with 3 planets as depicted in Figure 5 consists of 3 planets, 1 carrier, 1 sun gear and 1 ring gear or in total, 6 bodies. All the bodies can rotate except the ring gear which is fixed. Six bodies which can rotate (θ) and translate (in the $x-$ and $y-$directions) result in 18 generalized coordinates, which will also be the size of the $\ddot{\mathbf{q}}$-vector. The following is a list of 6 bodies:

1. Sun gear.
2. Planet gear 1.
3. Ring gear.
4. Carrier.
5. Planet gear 2.
6. Planet gear 3.

In the mathematical definition of the constraints, $\mathbf{r}$, describes the global position of the origin of the local coordinate system attached to a rigid body. A transformation matrix, $\mathbf{A}$, transforms a vector from local coordinates to global coordinates. A prime is added to a vector to indicate that the vector is defined in local coordinates, while a vector symbol with no prime attached, represents a vector in the global/inertial coordinate system. The following lists the 13 constraint equations (see Figure 5):

2 constraints fix the center of the sun gear to the ground (revolute joint):

$$\mathbf{\Phi}_{1-2} : \mathbf{r}_1 = \mathbf{0} \tag{6}$$

2 constraints fix the center of the carrier to the ground (revolute joint):

$$\mathbf{\Phi}_{3-4} : \mathbf{r}_4 = \mathbf{0} \tag{7}$$

2 constraints fix one of the endpoints of the carrier to the center of planet gear 1 using a revolute joint:

$$\mathbf{\Phi}_{5-6} : \mathbf{r}_4 + \mathbf{A}_4\mathbf{s}'_{4,P1} - \mathbf{r}_2 = \mathbf{0} \tag{8}$$

2 constraints fix the ring gear to the ground.

$$\mathbf{\Phi}_{7-8} : \mathbf{r}_3 = \mathbf{0} \tag{9}$$

1 constraint additionally prevents the ring gear from rotating.

$$\mathbf{\Phi}_{9} : \theta_3 = 0 \tag{10}$$

2 constraints fix one of the endpoints of the carrier to the center of planet gear 2 using a revolute joint.

$$\mathbf{\Phi}_{10-11} : \mathbf{r}_4 + \mathbf{A}_4\mathbf{s}'_{4,P2} - \mathbf{r}_5 = \mathbf{0} \tag{11}$$

2 constraints fix one of the endpoints of the carrier to the center of planet gear 3 using a revolute joint.

$$\mathbf{\Phi}_{12-13} : \mathbf{r}_4 + \mathbf{A}_4\mathbf{s}'_{4,P3} - \mathbf{r}_6 = \mathbf{0} \tag{12}$$

where:

$$\mathbf{0} = \begin{Bmatrix} 0 \\ 0 \end{Bmatrix} \quad \text{and} \quad \mathbf{s}_{4,P1} = \begin{Bmatrix} l_c/2 \\ 0 \end{Bmatrix} \tag{13}$$

and $\mathbf{s}_{4,P2}$ and $\mathbf{s}_{4,P3}$ can be found using a transformation matrix where the difference is that planet gears two and three are 120° and 240° apart away from planet gear number 1. The dimension l_c is illustrated in Figure 5. There are no gear constraints. Instead the forces that make the gear wheels rotate are evaluated by modifying the RHS of the equations of motion (5) as described in the following.

2.3 Gear tooth flexibility and applied forces

A flexible 2D multibody program has been made, which unlike a rigid model has gear tooth penetration as illustrated in Figure 7a. The details of this code is described in Jørgensen et al. (2014a) and shortly summarized here. A transformation matrix is defined as

$$\mathbf{A}(\theta) = \begin{bmatrix} \cos\theta & -\sin\theta \\ \sin\theta & \cos\theta \end{bmatrix}, \tag{14}$$

and the penetration depth $\mathbf{l_p}$ along the line of action for gear bodies i and j is

$$\mathbf{l_p} = \mathbf{A}_\mathrm{d}\mathbf{A}_\mathrm{s/p}\mathbf{v_n}\left[\rho_{b_i}(\theta_i - \theta_i^0 - \theta_d) + \rho_{b_j}(\theta_j - \theta_j^0 - \theta_d)\right], \tag{15}$$

where $\mathbf{A}_\mathrm{d}$ is a driver/carrier transformation matrix (using θ_d shown in Figure 5), $\mathbf{A}_\mathrm{s/p}$ is a transformation matrix from the direction shown using θ_d (Figure 5) to one of the three planets, e.g. 0°, 120° or 240°. The unit tooth surface normal vector $\mathbf{v_n}$ is a function of the pressure angle (typically $\alpha = 20°$ or $\alpha = 25°$), illustrated in Figure 6 and defined as

$$\mathbf{v_n} = \begin{Bmatrix} \sin(\alpha) \\ \cos(\alpha) \end{Bmatrix} \tag{16}$$

Gear tooth penetration is illustrated in Figure 7a. The time-differentiated penetration depth $\dot{\mathbf{l}}_\mathbf{p}$ is associated with damping and is calculated using

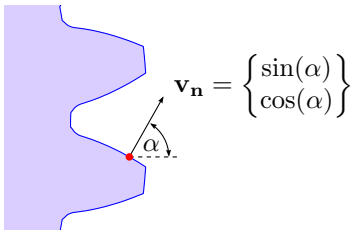

Figure 6: Unit tooth surface normal vector in the penetration direction as a function of gear tooth pressure angle α.

$$\dot{\mathbf{l}}_\mathbf{p} = \mathbf{A_d} \mathbf{A}_{\mathrm{s/p}} \mathbf{v_n} \left[\rho_{b_i} (\omega_i - \omega_d) + \rho_{b_j} (\omega_j - \omega_d) \right] \quad (17)$$

With stiffness coefficient k and damping coefficient d, gear tooth stiffness and damping forces are calculated using $\mathbf{F^k} = k\mathbf{l_p}$ and $\mathbf{F^d} = d\dot{\mathbf{l}}_\mathbf{p}$ respectively. Reaction forces are opposite of each other for bodies i and j and the force is applied to the $\mathbf{g}$-vector on the right hand side (RHS) of Equation (5). Additionally, these forces contribute to additional torque. A radial unit vector from center of sun to center of planet gear $\mathbf{v_r}$ is introduced. This radial unit vector $\mathbf{v_r}$ can be rotated 90° using the hat vector

$$\mathbf{v} = \begin{Bmatrix} x \\ y \end{Bmatrix}, \qquad \Rightarrow \qquad \hat{\mathbf{v}} = \begin{Bmatrix} -y \\ x \end{Bmatrix} \quad (18)$$

and the tangential gear tooth force is the spring and damping force sum projected into the tangential direction using the dot product $F_t^{\mathrm{k+d}} = \hat{\mathbf{v}}_\mathbf{r}^T (\mathbf{F^k} + \mathbf{F^d})$. Hence, the torque is $M = \rho_w F_t^{\mathrm{k+d}}$ where ρ_w is working circle radius. The total force and torque vector on the RHS of Equation (5) become

$$\mathbf{g_i^{Flex}} = \begin{Bmatrix} -k\mathbf{l_p} - d\dot{\mathbf{l}}_\mathbf{p} \\ -\rho_{w_i} F_t^{\mathrm{k+d}} \end{Bmatrix}, \qquad \mathbf{g_j^{Flex}} = \begin{Bmatrix} k\mathbf{l_p} + d\dot{\mathbf{l}}_\mathbf{p} \\ -\rho_{w_j} F_t^{\mathrm{k+d}} \end{Bmatrix} \quad (19)$$

The frictional force in the gear tooth contact is neglected in the multibody simulation due to the relative small size. The friction is the source of loss in the gear box, and also has an influence on the contact stress in the gear tooth. The friction is therefore included in the contact stress evaluation.

2.4 Gear tooth stiffness, base circle arc length and gear tooth forces

Figure 7 illustrates some important concepts in relation to gear geometry and the base circle arc lengths s_1 and s_2. With flexible connected bodies both gear wheels can penetrate each other. The gear tooth stiffness has been calculated using a Finite Element Method (FEM)

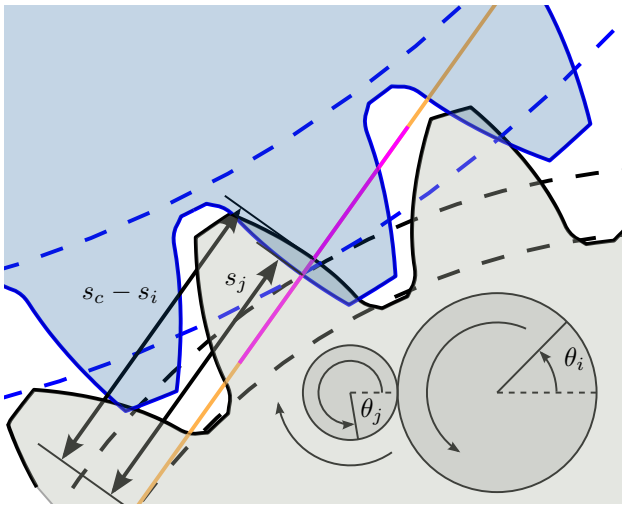

(a) Gear tooth model using flexible model. The result of the multibody program yields the angles θ_i and θ_j. From this, the base circle arc lengths s_i and s_j are calculated. A FEM-program (Multiphysics (1998-2012)) was used for obtaining stiffnesses, see details in Jørgensen et al. (2014a).

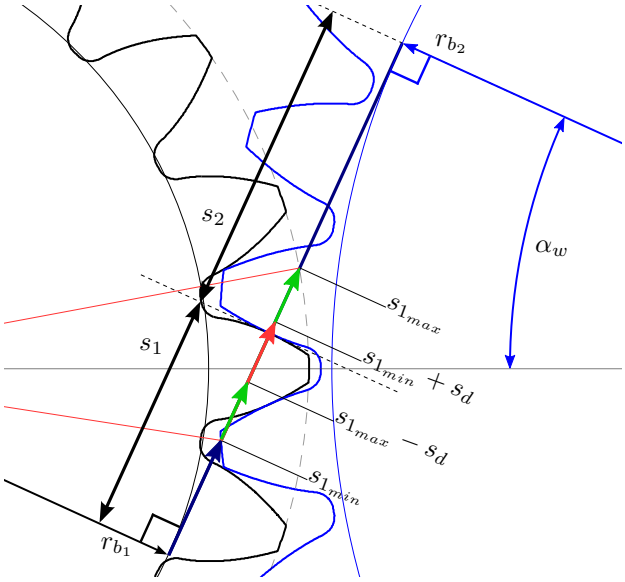

(b) Base circle arc length, s_1 and s_2 with line of action seen from the point of view of gear 1. Base circle radii are denoted r_b and working pressure angle is α_w. Green arrows indicate 2 teeth in contact (high stiffness) and the red arrow indicates 1 tooth in contact with the other gear.

Figure 7: Tooth penetration and estimation of equivalent stiffness from flexible multibody model. The sum of distances $s_1 + s_2 = s_c$ is a constant, see additional details in Pedersen and Jørgensen (2014).

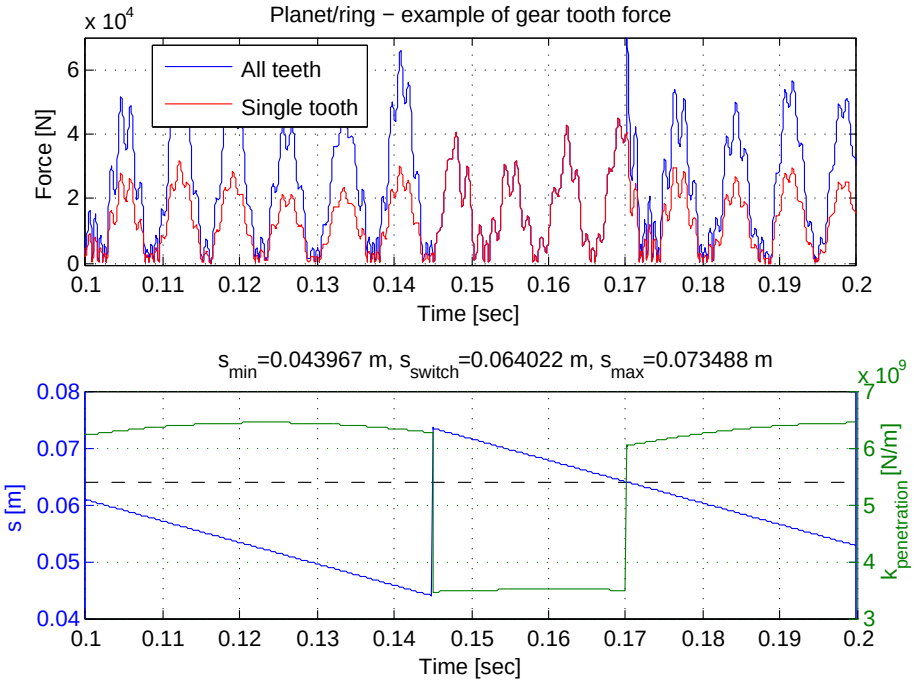

Figure 8: Top graph: The total gear tooth force is shown in blue, while the gear tooth force from a single gear (due to lower stiffness) is shown in red. When only one pair of teeth is in mesh, the red and blue curves are coinciding. The multibody program uses the blue curve, but for the fatigue analysis, the red (single-tooth contact) curve will be used. Lower graph: The base circle arc length of the inner gear (s_1 on Figure 7b) and corresponding FEM-stiffness.

package Multiphysics (1998-2012) and expressed as a function of an "average" angle or base circle arc length. Figure 7a shows gear tooth penetration (strongly exaggerated for illustrative purposes) and the average of s_i and s_j, is made equal to s_1 in Figure 7b, which is the contact point of two completely rigid gears in mesh. The FEM-model is used to calculate the stiffness at different contact points (Figure 9). In other words, the FEM contact point is located at a distance of s_1 from r_{b_1} (or at a distance of s_2 from r_{b_2}) and it is necessary to keep track of this location as the gears in the model rotate. Calculating the tooth stiffness at various locations is suggested as a good way to include additional realism, see Jørgensen et al. (2014a) for additional details.

Figure 7b shows that the base circle arc length (s_1 or s_2) represents the current rotation of both gear wheels as well as the gear tooth penetration depth of each gear tooth into the other gear(s) in mesh is a function of stiffness and tooth force. The sum of s_1 and s_2 is constant, but both distances change as a realistic dynamic model of the gear teeth requires this. By means of the gear tooth penetration depth, the "average" base circle arc length and the gear tooth stiffness, the total gear tooth force for all teeth is calculated and plotted in Figure 8. This figure shows both total gear tooth forces (used on the RHS of Equation (5)) as well as a fictive "single tooth force", including corresponding (lower graph) base circle arc length and tooth stiffness as a function of time.

A "fictive" single gear tooth force is required for fatigue analysis. The reason is that it is necessary to only look at one gear tooth at the time, even though sometimes the load is shared among two gear teeth. The problem is extensively described in Pedersen and Jørgensen (2014), but shortly explained the single gear tooth force is calculated as $F_t k_1/k_t$, where F_t is the total gear tooth force (sum of spring and damping forces), k_1 is the single gear tooth stiffness and k_t is the total gear tooth stiffness.

Figure 8 shows 0.2 seconds of simulation time and it shows whether 1 or 2 teeth are in mesh at a given time (high stiffness is when two gear teeth are in mesh and low stiffness of around $3.5{\cdot}10^9$ N/m is when only one gear tooth is in mesh). The figure shows that most of the time 2 gear teeth are in mesh, except in the interval $[0.145; 0.17]$ seconds.

The method used here for simulating the flexibility of the gear tooth contact has the advantage that it is rather simple, leading to acceptable computer simulation times. At the same time the highly non-linear nature of the contact is included. The frictional force

due to the sliding between the gear teeth is neglected in the multibody simulation, but later included in the estimation of the contact stress.

2.5 Gear tooth stresses in relation to fatigue analysis

The gear tooth stiffness properties is the same as in Jørgensen et al. (2014a) and the damping coefficient is estimated to $d = 40 \cdot 10^3$ Ns/m. The following two stress situations have been examined

1. Gear tooth bending failure: A FEM-program has been used for obtaining stresses in the situation where a unit force is applied to different contact points (defined as the base circle arc length).
2. Gear tooth surface failure: Hertzian stress assumption is applied and pure rolling contact of cylinder-on-cylinder is assumed. The maximum stress a little below the surface is calculated.

The details of the two approaches are elaborated below and the 8 cases illustrated in Table 1 are considered using increasing turbulence intensity (TI).

2.5.1 Gear tooth root bending failure

The gear tooth stresses are assumed to be linearly dependent on the magnitude of the gear tooth force obtained from the multibody program (from Figure 8). In other words, the gear tooth stresses are assumed to be the normal single gear tooth force multiplied by the polynomial function describing the relationship between stresses and base circle arc length (see Figure 9). Furthermore it is assumed that the maximum stress appears at the same point in the tooth root although this is not completely true, i.e. the point of maximum stress moves slightly.

2.5.2 Gear tooth surface stresses - pitting

Contact surface stresses are calculated as if two cylinders with radii equal to the base circle arc lengths are in contact. The cylinder length is the minimum gear facewidth, resulting in an ellipsoidal-prism pressure distribution as described in Norton (2000). Gear teeth are not only exerted to pure rolling but also to significant sliding which changes the stress state. This quickly becomes a complicated problem and therefore the complexity is significantly reduced by estimating the maximum von Mises stress using a simple average between a static and a dynamic loading coefficient from Norton (2000). This can be justified because the averaging stress coefficient is deemed not important to calculate exactly, since it is the same for all simulation results and because the objective is to study the relative change in fatigue damage in cases of increasing turbulence.

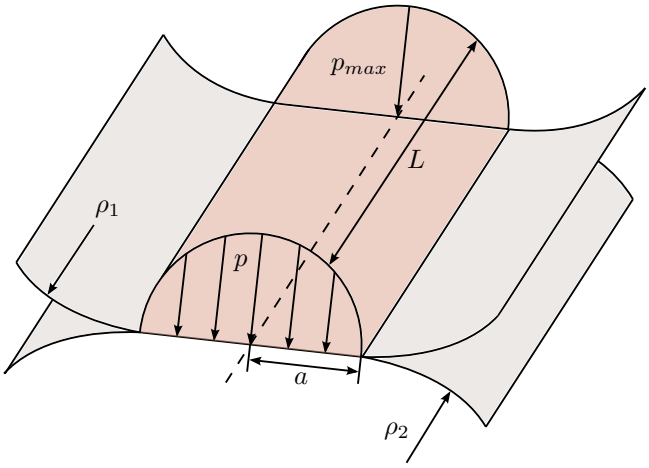

Figure 10: Hertzian pressure distribution with cylindrical contact using radii ρ_1 and ρ_2.

A cylindrical geometry constant B is defined as

$$B = \frac{1}{2}\left(\frac{1}{\rho_1} + \frac{1}{\rho_2}\right) \tag{20}$$

where ρ_1 and ρ_2 are the base circle arc lengths of the two gears in mesh (also illustrated in Figure 10, i.e. corresponding to the values of s_1 and s_2). The contact-patch half-width a is illustrated in Figure 10 and can be calculated as

$$a = \sqrt{\frac{2}{\pi}\frac{m_1 + m_2}{B}\frac{F}{L}} \tag{21}$$

using material constants $m_1 = m_2 = \frac{1-\nu^2}{E}$ where $\nu = 0.3$ is the Poisson ratio and $E = 210$ GPa is the Young's modulus. The gear tooth force calculated by the multibody program is denoted F. The maximum pressure/stress is

$$p_{max} = \frac{2F}{\pi a L} \tag{22}$$

The estimated Von Mises stress is taken as an average of a static and a dynamic coefficient (from Norton (2000)) and it is estimated to $\sigma = p_{max}\left(\frac{0.57+0.73}{2}\right) = 0.65\ p_{max}$. Because the relative fatigue damage is important, it is deemed that it is not that important whether 0.6, 0.65 or 0.7 is used but 0.65 can be justified, at least to illustrate the proposed method. The maximum von Mises stress is found subsurface Norton (2000) leading to fatigue micro-cracks and development of pitting. The von Mises stress is used together with a rainflow-counting program that has been verified against a similar tool that is part of FLEX 5.

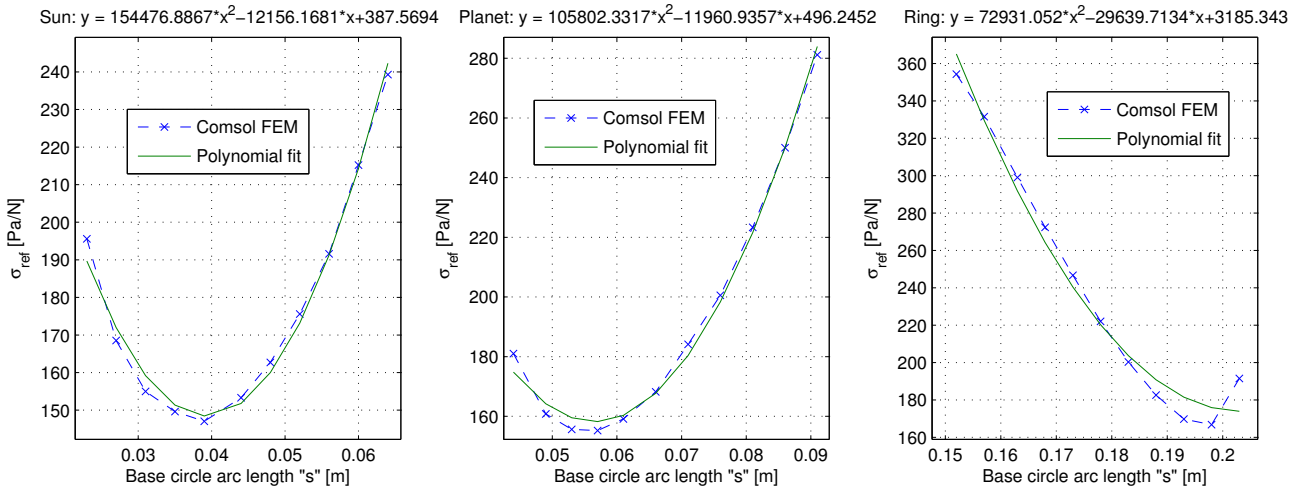

Figure 9: Maximum von Mises stress at gear tooth for a unit force (1 N) applied at a given base circle arc length distance "s". A second order polynomial fit approximates the FEM-results well, for the base circle arc length intervals of interest.

3 Implementation details

The simulation model has been described. The objective, to calculate data for representing the lifetime fatigue, is difficult. Relatively short timeseries of simulation results made with very small timesteps are used on a much larger time-scale by using "time scaling"-factors. It is necessary to explain this and also how the S–N (Wöhler) curve parameters are chosen.

- Section 3.1 describes the time-factor considerations used for the rainflow counting algorithm for matching operational hours from the Weibull-distribution.
- Section 3.2 describes some S–N (Wöhler) curve considerations, i.e. material fatigue characteristics.

3.1 Adjusting time-factors due to different gear teeth in contact

Simulation time is 30 seconds (computation time is 10-15 hours per run). For fatigue-calculations the simulation time must be "upscaled" to the real number of operational hours given by the Weibull distribution for this particular site (shown in Table 1). Table 2 shows a simple (unadjusted/naive) time-factor calculation, i.e. when using the rainflow-counting algorithm, the number of cycles must be multiplied by this number to get an idea of the accumulated fatigue damage over the lifetime. The time-factor is calculated as the operational hours times 3600 seconds, divided by the simulation time in seconds. It is assumed that everything within those 30 seconds of simulation time is representative for the whole lifetime. Due to the high stiffness of the gear teeth the timestep is rather small and the simulation time limit depends on computation time and memory.

The sun has 20 teeth, the planets have 35 teeth and the ring 91 teeth. In other words "on average" those 30 seconds of simulation time and corresponding von Mises stresses, correspond to 600 simulation seconds for one specific sun gear, 1050 simulation seconds for one specific planet gear and 2730 seconds for one specific ring gear. The time-factor will simply be reduced by the number of gear teeth. Another important thing to consider is that every full rotation of a tooth on the sun gear, is met by teeth from the three planet gears (see Figure 5). Therefore the fatigue from the calculated stresses for teeth in contact must be added together. Instead of having three 30-second simulations this situation corresponds to making a fatigue calculation on a longer 90-second simulation. The same idea for the sun gear can also be used for a full ring gear cycle, which "sees" 3 planet planet/ring gear connections. One rotation of the planet gear however corresponds to "only" a 60-second simulation because one gear tooth will see another tooth from the ring and from the sun gear at all times. Tooth-adjusted time-factors are summarized in Table 3.

3.2 S–N-curve details

Realistic S–N-curves for these particular gear teeth are difficult to obtain and therefore the endurance limit as well as the slope must be estimated. It is known from Norton (2000) that the maximum von Mises stress is slightly below the surface which is therefore expected

Wind speed [m/s]	6	8	10	12	14	16	18	20
In operation [hours]	45418	31900	16320	6189	1751	370	58	7
Time-factor (TF)	5450160	3828000	1958400	742680	210120	44400	6960	840

Table 2: Time scaling for 30 seconds simulation time (no adjustment).

Wind speed [m/s]	6	8	10	12	14	16	18	20
In operation [hours]	45418	31900	16320	6189	1751	370	58	7
TF_s (×20, 90 sec)	272508	191400	97920	37134	10506	2220	348	42
TF_p (×35, 60 sec)	155719	109371	55954	21219	6003	1269	199	24
TF_r (×91, 90 sec)	59892	42066	21521	8161	2309	488	76	9

Table 3: Adjusted time scaling for teeth on different gears. Last three rows is the fatigue time-factor for a sun, planet or a ring gear tooth. Because the stresses (and gear tooth forces) are comparable, a fatigue calculation does not need to be done on all individual planets.

to decrease the endurance limit. S–N-parameters (see Figure 4) will be estimated based on Hirsch et al. (1987); Boyer (1986) using the two points in Table 4. The following expression is obtained (see Figure 4)

$$s(N) = s_0 N^{\frac{-1}{m}} \tag{23}$$

where $s_0 = 28.9$ GPa and $m = 3.4$, while σ_e is the endurance limit in MPa. A large uncertainty is involved when choosing material and S–N parameters, however for illustrative purposes the endurance limits in Table 5 are chosen. The endurance limit works as a threshold which effectively can neglect fatigue problems if raised just slightly to e.g. 850-1000 MPa. Table 5 shows that the sun and planet gears have the same, relatively high, endurance limit.

	N [cycles]	σ [MPa]
P_1	$3 \cdot 10^4$	1400
P_2	$1 \cdot 10^6$	500

Table 4: S–N curve parameters using two points (P_1 and P_2 can be seen in Figure 4).

	σ_e [MPa]
Sun gear	800
Planet gear	800
Ring gear	550

Table 5: Endurance limits for S–N curve.

Adjusting the S–N curve and endurance limits makes a great difference in the results. If all parameters are the same (e.g. endurance limit of 550 MPa), results clearly illustrate that the sun gear is most exposed to fatigue. A plausible explanation is that three planet gear teeth are acting on the sun and the sun gear has only 20 teeth. Results also clearly show that the ring gear is the least subjected to fatigue. Although it is constantly exposed to contact from three planet teeth, it has a total of 91 teeth and hence the lowest timefactor.

4 Results

Results are divided into a section dealing with root bending failure and surface stresses (pitting).

4.1 Root bending failure

The maximum gear tooth stresses are expected using a mean wind speed of 20 m/s. However the results in Figure 11 using TI=10% indicate that the maximum stresses at the gear root is approximately 60 MPa, which is clearly below the endurance (or fatigue) limit. Even though the maximum stress would be higher for increasing turbulence intensities, it is not considered a problem because the endurance limit is much higher. It can be concluded that for these particular gear teeth, no fatigue damage will happen at the root.

4.2 Surface stresses / pitting

The maximum von Mises stress using $\bar{U} = 20$ m/s and TI=10% is found to be 6-700 MPa which will contribute to fatigue damage. Figure 12 is an example of the planet/ring stress level for a 30-second simulation. We select a specific location on a gear tooth (i.e. choose a corresponding s-value, see Figure 7) and draw a vertical line using the results from Figure 12b and process the von Mises stress using a rainflow-counting algorithm and the S–N-curve data from Table 4.

4.2.1 Average von Mises stress

Figure 7a illustrates how the base circle arc length s is measured and Table 6 indicates important base circle arc lengths (the middle value for s is the interface/switch-point between a single and two teeth

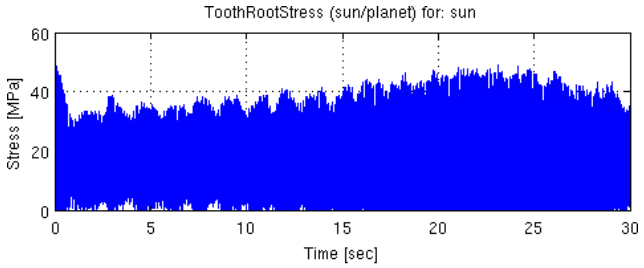

(a) Sun/planet.

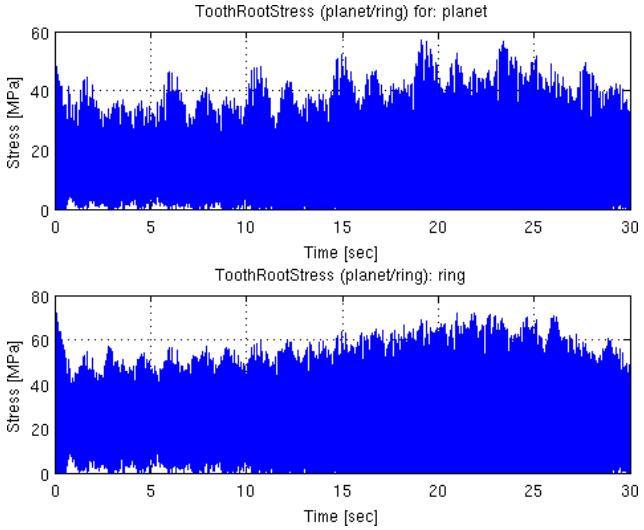

(b) Planet/ring.

Figure 11: Gear tooth root stresses using TI=10% and mean wind speed $\bar{U} = 20$ m/s.

s [m]	0.0243	0.0382	0.0538
Teeth in contact	2	-	1

(a) Sun/planet

s [m]	0.044	0.064	0.0735
Teeth in contact	2	-	1

(b) Planet/ring

Table 6: Switch between single and multiple teeth in mesh (the planet/ring delimiters are also shown in Figure 12, making it easier to see whether one or two teeth are in mesh).

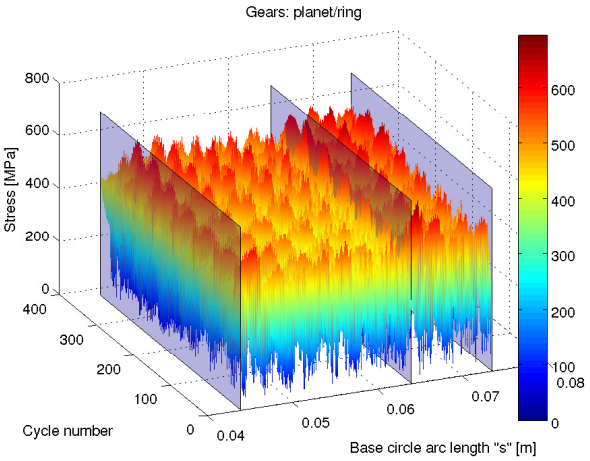

(a) 3 transparent plates are inserted, left region shows two-teeth contact and right region shows single-tooth contact.

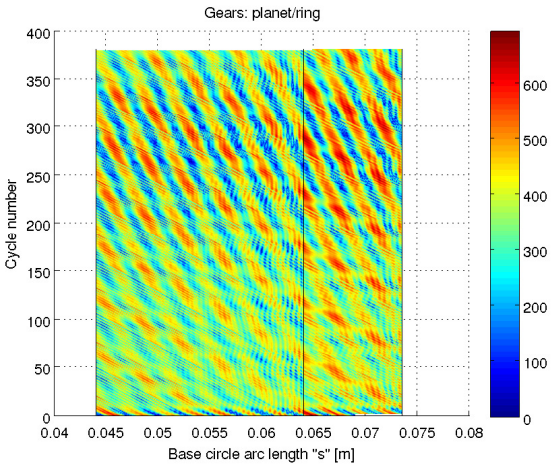

(b) 2D plot of (a) including both regions (black vertical lines). Mean wind speed is 20 m/s, TI=10%.

Figure 12: Estimated von Mises stress for 30 second simulation time, as a function of base circle arc length "s". For this to be plotted properly, interpolated von Mises stress values are used.

in mesh). In relation to sun/planet and planet/ring gear tooth contact, it is defined to measure the base circle arc length from the "inner gear", i.e. sun/planet gear tooth contact, s is measured relative from the sun base circle and for planet/ring gear tooth contact s is measured relative from the planet base circle. One could also express the same base circle arc length measured from the "outer gear", so this is a matter of choice or definition. A consequence of this choice is that low s-values means tooth contact is close to the "inner gear" and vice versa. In addition low s-values imply high stiffness because two gear teeth is in mesh and vice versa for high s-values where only a single tooth is in mesh.

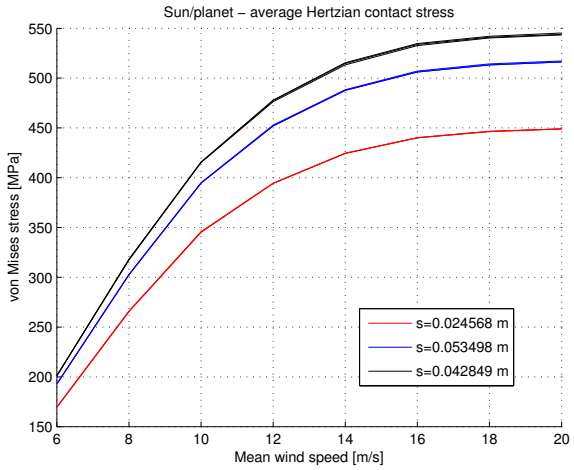

(a) Sun/planet.

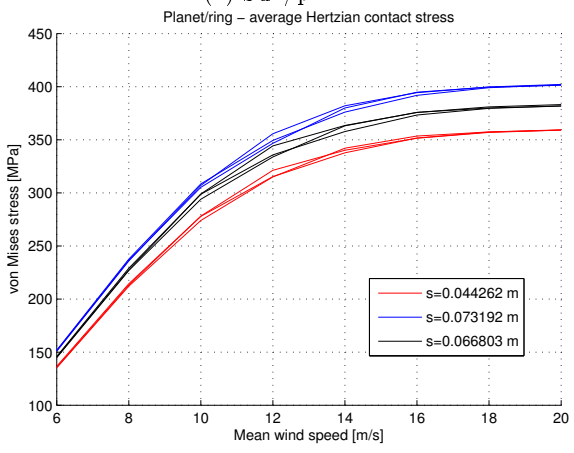

(b) Planet/ring.

Figure 13: Average von Mises contact stress for TI=10%.

Figure 12 shows an example of the stresses calculated for a simulation with indication of 3 different base circle arc length locations. The multibody program only calculates the gear tooth forces as a function of the dynamics of the whole system and that system does not guarantee to store the results at exactly any given point (which is necessary for a fatigue calculation). For that reason, interpolation has been used and because the stiffness is very high, the timestep is low causing long computation times. Each simulation requires around 5-10 GB of memory for only 30 seconds. With high stiffness and low timestep it is assumed that interpolation of gear tooth forces is a good solution for calculating the stresses at specific locations. The pattern in Figure 12 indicates that the interpolated stresses are not "random". The pattern indicates that regions of high and low stresses are a repetitive and cyclic phenomenon, as a result of using realistic non-linear stiffness.

Because interpolation is used, the endpoints of the base circle arc length distances are not applicable for interpolation. There are too few stress results here, i.e. only seldom the multibody program calculates the solution exactly at the endpoints. Two of the base circle arc lengths in Figure 12 are close to the endpoint values in Table 6 but not completely the same. This also applies to Figure 13. The location indicating a switch from one to two gears in mesh from Table 6 (s=0.0382 m and s=0.064 m) is excluded because such an interpolation yields unpredictable and unusable stresses. On one side of the interpolation, two teeth are in mesh and on the other side, only a single tooth is in mesh with the other gear.

From Figure 13 it can be concluded that the average stresses are lowest for low values of s (the two red curves). This is a region with high stiffness due to the fact that two teeth are in mesh at the same time. Additionally, a black curve is added to both graphs in Figure 13. This line indicates the contact point of the two working circles, i.e. the pitch point where only rolling appears (everywhere else sliding takes place). At this point only a single tooth is in mesh and that explains the higher stresses. Figure 12 shows that the stresses are not the same everywhere, i.e. it is ambiguous which value of s yields the maximum average stresses for both sun/planet and planet/ring results.

Figure 13 resembles a behavior similar to those found using a rigid multibody model in Jørgensen et al. (2014b). It assumed that multiple flexible planets on one hand decrease the gear tooth force because additional planets share the load. On the other hand, the gear tooth force is probably increased because not all springs and dampers are aligned equally (especially not when addendum modification is used). If one of the planets tries to rotate in one direction, one of the other planets could try to rotate in another direction due to the spring/damper force. With high stiffness these spring and damper forces are not negligible and cause the three planets to act against each other while trying to rotate the sun and ring gears at the same

time. This can cause severe peak loads.

4.2.2 Accumulated rainflow counting results

Figure 14 shows an example of processing the 30 seconds sun/planet von Mises stress calculation results through the RFC-code. Figure 14a shows the stress range for each of the 6-20 m/s mean wind speed bins. It can be seen that the change from 6-8 and 8-10 m/s is huge in comparison with the change from e.g. 16-18 or 18-20 m/s. Figure 14b is the cumulative number of full cycles, using the time factor for the sun gear (TF_s from Table 3). Both figures illustrate that if the endurance limit exceeds around 850-1000 MPa, then fatigue and surface pitting of the sun gear is not a problem. Similar observations can be made for the planet and ring gears.

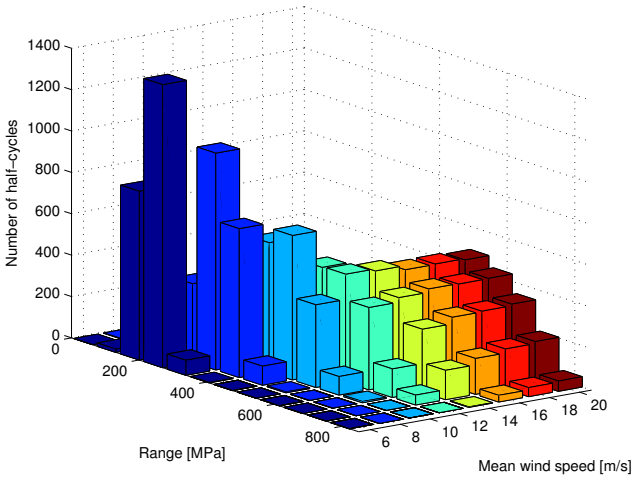

(a) Half cycle count, 6-20 m/s mean wind speed.

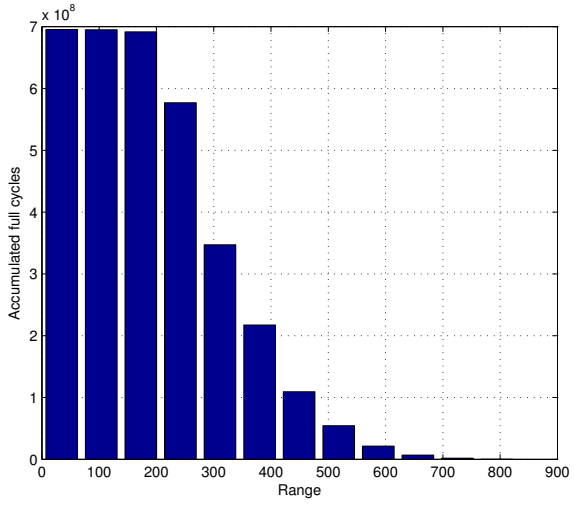

(b) Cumulative full cycle count (using TF_s).

Figure 14: Example of rain flow counting result using TI=10%.

4.2.3 Cumulative fatigue damage due to increased turbulence

The IEC 61400-1 standard about design requirements for wind turbines specifically operate with 3 classes for turbulence intensity: 12%, 14% and 16%. Turbulence intensity depends on e.g. surface roughness i.e. how many disturbances are present from e.g. trees/buildings etc and also hub height. In other words, the turbulence intensity is generally lower for offshore wind turbines (undisturbed) when compared to that of landbased wind turbines. With increasing altitude, the flow is generally also less disturbed leading to less "average" turbulence.

Table 7 shows the contribution of fatigue damage at different mean wind speeds and the total fatigue damage on each gear wheel. The star after the planet denotes average fatigue damage on each of the three planets. It can be concluded that generally wind speeds of 14-16 m/s contribute the most to fatigue. The explanation is that even though the stress range count is higher at higher wind speeds, the wind rarely blows above 16 m/s.

	8%	10%	12%	14%	16%	18%	20%
Sun	0.65	0.69	0.75	0.85	1.10	1.60	2.00
Planet*	0.12	0.13	0.14	0.16	0.21	0.30	0.38
Ring	0.05	0.05	0.05	0.05	0.07	0.10	0.11

Table 8: Total fatigue damage as a function of increasing turbulence.

Table 8 shows total cumulative damage as a function of increasing turbulence. Assuming that the material data and S–N-curve data are realistic, gear tooth surface pitting at the sun gear is expected if the average turbulence exceeds 14-16%. The ring gear with an endurance limit of only 550 MPa is still not exposed to as much fatigue damage as the planet gear with 800 MPa endurance limit. With 91 teeth, the ring gear is the most durable to pitting caused by surface fatigue but with lowered endurance limit, this result was not obvious. However, with 500 MPa endurance limit for the ring gear, the planet gear becomes least subject to fatigue damage. Figure 15 graphically summarizes the lifetime fatigue calculation results, using the flexible multibody model and Hertzian contact stress assumption. This gearbox is only deemed usable if the representative turbulence level is below 15%. Accumulated damage increases quickly for increasing turbulence intensity above approximately 16-17%. Results suggest that the sun gear with few teeth, will be the most important to protect by ensuring correct maintenance and regular inspections. Possibly extra care of the sun gear must also be taken under manufacturing. The results

	6 m/s	8 m/s	10 m/s	12 m/s	14 m/s	16 m/s	18 m/s	20 m/s	Σ
Sun	0	0	0	0	0.2185	0.3727	0.0869	0.0132	0.69
Planet*	0	0	0	0	0.0416	0.0710	0.0166	0.0025	0.13
Ring	0	0	0	0.0116	0.0177	0.0125	0.0028	0.0004	0.05

Table 7: Example of accumulated fatigue damage using TI=10% (* means average of 3 planets).

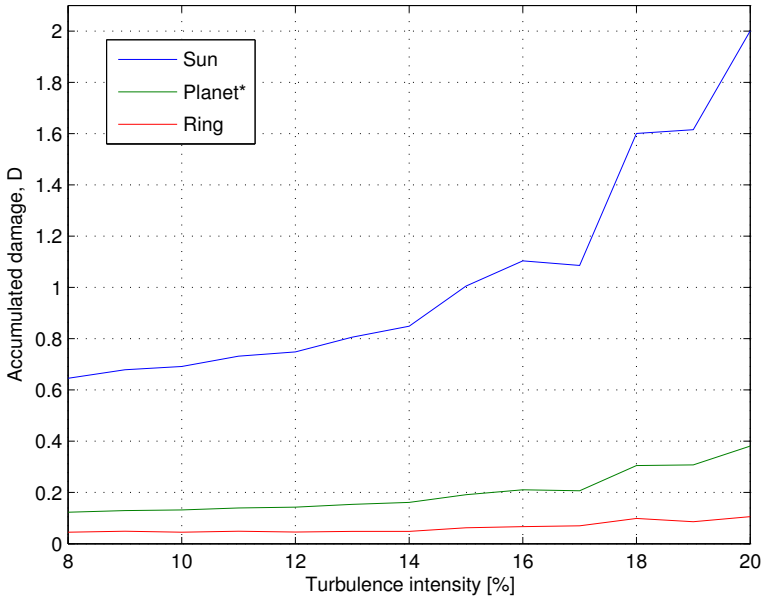

Figure 15: Accumulated fatigue on sun, planet and ring gears for lifetime operation (20 years).

finally demonstrate the importance of specifying a material and surface/heat treatment process leading to a high endurance limit, for the sun gear.

5 Conclusions

This paper focuses on investigating fatigue problems in relation to gear teeth in a planetary gearbox. The Weibull cumulative distribution function and Palmgren-Miner linear damage hypothesis is used together with

1. A method for estimating gear root stresses.
2. A method involving Hertzian contact stress assumption.

It is found that the investigated 500 kW wind turbine gearbox has no fatigue-problems related to gear tooth root bending. The Hertzian contact stress assumption implies calculating the maximum von Mises stresses slightly under the gear tooth surface. Fatigue damage occurs under the assumption of using an endurance limit of 800 MPa for the sun and the planet gear wheels. The interpretation of this result is that fatigue just below the gear tooth surface can lead to gear tooth surface pitting, which eventually increases the risk of gearbox failure. Furthermore it can be concluded that:

- The average von Mises stress flattens out in the high mean wind speed region, i.e. in the interval of mean wind speeds approximately between 15-20 m/s, the stresses are not much higher than at 15 m/s. This behavior resembles that of a typical power-curve for a wind turbine and it also resembles a similar result published in Jørgensen et al. (2014b).

- The stresses at specific locations have been calculated using interpolation and it can clearly be seen that the von Mises stress on a single gear tooth in the region where two gear teeth are in mesh (low base circle arc lengths), are lower than in the region where only a single tooth is in mesh. Specifically it can be concluded that the stresses at the working circle/pitch point and for higher base circle arc lengths are higher, than at points specified by low base circle arc lengths. The gear tooth stresses on a specific place on the tooth are lower in the region where two gear teeth share the load, when compared to the case where only a single gear tooth must take the whole load.

- When estimating the effect of turbulence on gear tooth surface pitting, a marginal increase in turbulence in the high turbulence region relatively contributes much more to accumulated fatigue damage, than the same increase in low turbulence regions.

A practical perspective of these results suggests that for low turbulence intensities, wake effects (turbulence generated from other wind turbines in a wind farm) are not deemed important as a cause of gearbox failure due to pitting caused by subsurface cracks.

It is common to assume that the turbulence intensity for offshore wind turbines is lower than that of similar landbased wind turbines (because these are located near obstacles such as trees, buildings, uneven terrain etc which increase the turbulence). Our results suggest particular attention to pitting as a cause of gearbox failure, should be taken when making wind turbine layouts of wind farms in regions with high turbulence.

Acknowledgments

This research was supported by DSF (Danish Council for Strategic Research) grant 09-071588.

References

Boyer, H. E. *Atlas of fatigue curves*. ASM International, 1986.

Dong, W., Xing, Y., Moan, T., and Gao, Z. Time domain-based gear contact fatigue analysis of a wind turbine drivetrain under dynamic conditions. *International Journal of Fatigue*, 2012. doi:10.1016/j.ijfatigue.2012.10.011.

Fernandes, P. and McDuling, C. Surface contact fatigue failures in gears. *Engineering Failure Analysis*, 1997. 4(2):99–107. doi:10.1016/S1350-6307(97)00006-X.

Géradin, M. and Cardona, A. *Flexible multibody dynamics: a finite element approach*. John Wiley, 2001.

Hansen, K. S. and Larsen, G. C. Database of wind characteristics: http://www.winddata.com. 1997-2011. URL http://www.winddata.com/.

Hasager, C. B., Rasmussen, L., Peña, A., Jensen, L. E., and Réthoré, P.-E. Wind farm wake: The horns rev photo case. *Energies*, 2013. 6(2):696–716. doi:10.3390/en6020696.

Haug, E. J. *Computer Aided Kinematics and Dynamics of Mechanical Systems: Vol. I: Basic Methods*. Allyn and Bacon, 1989.

Heege, A., Betran, J., and Radoveic, Y. Fatigue load computation of wind turbine gearboxes by coupled finite element, multi-body system and aerodynamic analysis. *Wind Energy*, 2007. 10(5):395–413. doi:10.1002/we.226.

Hirsch, T., Wohlfahrt, H., and Macherauch, E. Fatigue strength of case hardened and shot peened gears.(retroactive coverage). *Shot Peening: Science, Technology*, 1987. pages 547–560.

Jørgensen, M. F., Pedersen, N. L., and Sørensen, J. N. Comparison and implementation of a rigid and a flexible multibody planetary gearbox model. *Modeling, Identification and Control*, 2014a. 35(2):59–77. doi:10.4173/mic.2014.2.1.

Jørgensen, M. F., Pedersen, N. L., Sørensen, J. N., and Paulsen, U. S. Rigid matlab drivetrain model of a 500 kw wind turbine for predicting maximum gear tooth stresses in a planetary gearbox using multibody gear constraints. *Wind Energy*, 2014b. 17(11):1659–1676. doi:10.1002/we.1660.

Madsen, P. *Recommended practices for wind turbine testing and evaluation; 3. Fatigue Loads*, volume 2. 1990.

Mann, J. Wind field simulation. *Probabilistic Engineering Mechanics*, 1998. 13(4):269–282. doi:10.1016/S0266-8920(97)00036-2.

Miner, M. A. Cumulative damage in fatigue. *Journal of applied mechanics 12, no. 3*, 1945. pages 159–164.

Molinas, M., Suul, J. A., and Undeland, T. Extending the life of gear box in wind generators by smoothing transient torque with statcom. *IEEE Transactions on Industrial Electronics*, 2010. 57(2):476–484. doi:10.1109/TIE.2009.2035464.

Multiphysics, C. www.comsol.se. 1998-2012.

Musial, W., Butterfield, S., and McNiff, B. Improving wind turbine gearbox reliability. In *Proceedings of the European Wind Energy Conference*. 2007.

Niederstucke, B., Anders, A., Dalhoff, P., and Grzybowski, R. Load data analysis for wind turbine gearboxes. *Final Report of Enhanced Life Analysis of Wind Power Systems*, 2003.

Nikravesh, P. E. *Computer-Aided Analysis of Mechanical Systems*, volume 186. Prentice Hall, 1988.

Norton, R. L. *Machine Design: An Integrated Approach, 2nd ed.* Prentice-Hall, 2000.

Palmgren, A. Die lebensdauer von kugellagern. *Zeitschrift des Vereins Deutscher Ingenieure 68.14*, 1924. pages 339–341.

Pedersen, N. L. and Jørgensen, M. F. On gear teeth stiffness evaluation. *Computers and Structures, vol. 135, p. 109-117.*, 2014. doi:10.1016/j.compstruc.2014.01.023.

Schlechtingen, M., Santos, I., and Achiche, S. Wind turbine condition monitoring based on scada data using normal behavior models. *Applied Soft Computing*, 2013. 13:259–270. doi:10.1016/j.asoc.2012.08.033.

Seguro, J. and Lambert, T. Modern estimation of the parameters of the weibull wind speed distribution for wind energy analysis. *Journal of Wind Engineering and Industrial Aerodynamics*, 2000. 85(1):75 – 84. doi:10.1016/S0167-6105(99)00122-1.

Shabana, A. A. *Dynamics of Multibody Systems*. Wiley & Sons, 1989.

Smolders, K., Long, H., Feng, Y., and Tavner, P. Reliability analysis and prediction of wind turbine gearboxes. In *European Wind Energy Conference*. 2010.

Tronæs Frandsen, S. *Turbulence and turbulence-generated structural loading in wind turbine clusters*. Risø National Laboratory, 2007.

Vasudevan, A. K., Sadananda, K., and Glinka, G. Critical parameters for fatigue damage. *International Journal of Fatigue*, 2001. 23(SUPP/1):39–53. doi:10.1016/S0142-1123(01)00171-2.

Veers, P. S. Three-dimensional wind simulations. *Sandia Report, SAND-0152*, 1988.

Øye, S. *Various FLEX 5 documentation*. DTU Mechanical Engineering, 2001.